Filtered-backprojection reconstruction for a cone-beam computed tomography scanner with independent source and detector rotations

Simon Rit[a)]
Université de Lyon, CREATIS, CNRS UMR5220, Inserm U1044, INSA-Lyon, Université Lyon 1, Department of Radiation Oncology, Centre Léon Bérard, 28 rue Laennec, Lyon 69008, France

Rolf Clackdoyle
Laboratoire Hubert Curien, CNRS and Université Jean Monnet (UMR5516), 18 rue du Professeur Benoit Lauras, Saint Etienne F-42000, France

Peter Keuschnigg and Philipp Steininger
Institute for Research and Development on Advanced Radiation Technologies (radART), Paracelsus Medical University, Strubergasse 16, Salzburg 5020, Austria and medPhoton GmbH, Strubergasse 16, Salzburg 5020, Austria

(Received 5 October 2015; revised 12 February 2016; accepted for publication 22 March 2016; published 13 April 2016)

Purpose: A new cone-beam CT scanner for image-guided radiotherapy (IGRT) can independently rotate the source and the detector along circular trajectories. Existing reconstruction algorithms are not suitable for this scanning geometry. The authors propose and evaluate a three-dimensional (3D) filtered-backprojection reconstruction for this situation.
Methods: The source and the detector trajectories are tuned to image a field-of-view (FOV) that is offset with respect to the center-of-rotation. The new reconstruction formula is derived from the Feldkamp algorithm and results in a similar three-step algorithm: projection weighting, ramp filtering, and weighted backprojection. Simulations of a Shepp Logan digital phantom were used to evaluate the new algorithm with a 10 cm-offset FOV. A real cone-beam CT image with an 8.5 cm-offset FOV was also obtained from projections of an anthropomorphic head phantom.
Results: The quality of the cone-beam CT images reconstructed using the new algorithm was similar to those using the Feldkamp algorithm which is used in conventional cone-beam CT. The real image of the head phantom exhibited comparable image quality to that of existing systems.
Conclusions: The authors have proposed a 3D filtered-backprojection reconstruction for scanners with independent source and detector rotations that is practical and effective. This algorithm forms the basis for exploiting the scanner's unique capabilities in IGRT protocols. [http://dx.doi.org/10.1118/1.4945418]

Key words: image-guided radiotherapy (IGRT), three-dimensional (3D) imaging, cone-beam computed tomography (CT), tomographic reconstruction, filtered-backprojection algorithm, offset field-of-view

1. INTRODUCTION

The installation of imaging devices in radiotherapy rooms has initiated the growth of a new field, image-guided radiotherapy (IGRT),[1,2] which has become a crucial part of contemporary radiotherapy. Cone-beam computed tomography (CT) has significantly contributed to IGRT and it is today the main imaging modality for IGRT.[3] Cone-beam CT images are easy to compare with the treatment planning image which, in most hospitals, is acquired on a diagnostic CT scanner and is therefore a three-dimensional (3D) image of the same modality.

Most cone-beam CT scanners for IGRT are fixed to the gantry of a linear accelerator. Because they use the rotation system of the treatment machine, the x-ray images are acquired in the reference frame of the treatment plan which simplifies the treatment guidance. The drawbacks are a maximum rotation speed of about one minute per rotation, no choice in the field-of-view (FOV) center unless the patient table is translated, gantries in proton therapy that can only perform a partial revolution and limited flexibility in intradelivery IGRT protocols. The FOV is defined in this work as the region of space that is within the imaging zone (defined by the source and the detector) for every source position during the full 360° scan.

Recently, another cone-beam CT scanner, the *ImagingRing* (Fig. 1), has been developed by medPhoton, a spin-off company of Paracelsus Medical University (Salzburg, Austria). The name comes from the rotation system which is a ring attached to the patient couch. The ring can translate longitudinally along the patient table top under robotic control to cover all relevant anatomical regions. The kilovolt (kV) source and the flat panel detector are fixed to the ring and can rotate independently by more than 460° around the patient. The design choices of this system have been made to provide more versatile imaging configurations. The system can not only be used in combination with linear accelerators for conventional photon therapy but also in treatment rooms without rotation

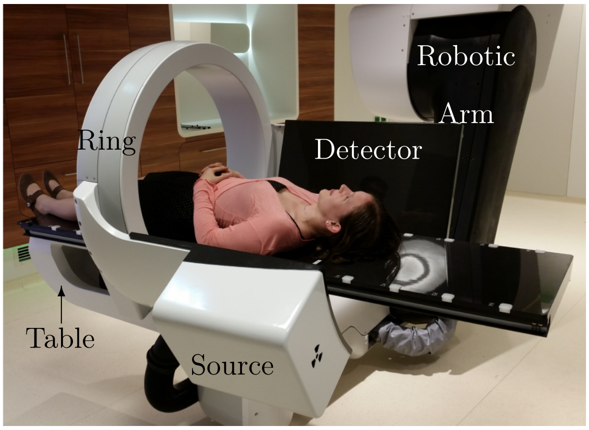

FIG. 1. Photograph of the prototype ImagingRing installed at MedAustron (Austria).

system, such as operating rooms for brachytherapy and surgery, or hadron therapy rooms with a fixed beam direction.

The geometry of most cone-beam CT scanners with a flat panel detector is such that for all angular positions of the system, the shortest line from the source to the detector intersects the axis of rotation. This geometry is called the *conventional geometry* in the following. With the ImagingRing, the independent rotations of the source and the detector, combined with dynamic x-ray collimation jaws, enable source and detector trajectories whose FOV is not centered on the center-of-rotation. This is clinically useful because the area of interest is typically not at the center-of-rotation of the scanner. If the FOV is offset with respect to the center-of-rotation, the detector is tilted with respect to the conventional geometry while, unlike the work of Grangeat *et al.*,[4] maintaining the axis of rotation parallel to the plane of the detector. This geometry has been previously studied in two-dimensional (2D) systems for a fixed tilt of the detector[5] and we have recently presented an extension for the ImagingRing,[6] i.e., with tilts that vary with the source position. A follow-up study was published by the same group[7] but the source-to-detector distance was fixed in their geometry which is not the case for the circular source trajectory of the ImagingRing.

In this paper, we further study CT reconstruction for the ImagingRing. The geometry and possible trajectories are reviewed. The previous reconstruction algorithm[6] is summarized and extended to three dimensions. The new 3D algorithm is evaluated on simulated data and compared to the Feldkamp algorithm[8] before being applied to a real dataset acquired on a prototype ImagingRing.

2. MATERIALS AND METHODS

2.A. ImagingRing

A first prototype ImagingRing has been installed at MedAustron, the Austrian Ion Therapy and Cancer-Research Centre Project (Fig. 1). Two arms are mounted on the ring to hold the x-ray source and the flat panel detector. These two arms can rotate independently to any angular position along the ring's 360° circular arc and each arm has a rotation range of more than 470°, which provides the flexibility to focus the scan on an off-center FOV as described in more detail below. The source and the detector positions along this ring are the two degrees-of-freedom (DOFs) of the scanner that will be used in this study while the third one, the longitudinal position of the ring with respect to the table, will be held constant.

2.B. Source and detector trajectories

Let $\mathbf{x}=(x,y,z)$ be a point in space with x, y, and z the coordinates of a 3D Cartesian coordinate system. The circular trajectory of the source is assumed to be in the $z=0$ plane, with a radius R, centered on the origin $\mathbf{o}=(0,0,0)$. The source position along its circular trajectory is denoted $\mathbf{s}_\beta=(-R\sin\beta,R\cos\beta,0)$ with β the angle between the y-axis and $\mathbf{s}_\beta$, measured positively in the counter-clockwise direction relative to the y-axis.

The geometry of the system in the plane $z=0$ is illustrated in Fig. 2. The detector follows a circular trajectory at a distance R_D from the common center-of-rotation $\mathbf{o}$. The flat detector of the ImagingRing can rotate independently from the source, i.e., it can be tilted by an angle τ with respect to the conventional geometry, measured positively in the counter-clockwise direction relative to the source-to-center line. The only constraint on τ is set by the ability of the collimation jaws to adjust the x-ray beam to the detector position. The detector angle τ is limited to the range $(-43°,51°)$. The detector plane is therefore spanned by the vectors $(\cos(\beta+\tau),\sin(\beta+\tau),0)$ and $(0,0,1)$. Let (u,v) denote the 2D coordinates along the axes of the detector with the (u,v) origin at the point of tangency $(R_D\sin(\beta+\tau),-R_D\cos(\beta+\tau),0)$ with the ring of radius R_D as indicated $(u=0)$ in Fig. 2. Unlike some conventional cone-beam CT systems where the detector can translate in the u direction to adjust the FOV size,[9] the position of the detector is fixed in this plane but uncentered (by design) along the u coordinate, with limits $[u_{\min},u_{\max}]$ and $[-v_{\max},v_{\max}]$ along the u and v axes, respectively.

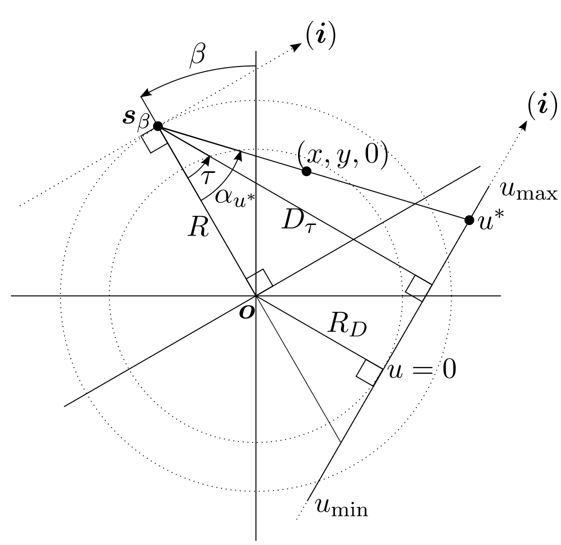

FIG. 2. Geometry of the central slice of the ImagingRing. Point $\mathbf{i}$ is in the central slice but outside of this drawing, at the intersection between the two lines where $(\mathbf{i})$ is indicated.

The detector tilt τ is a user parameter that can vary with source angle β. This DOF, in combination with the adjustable collimator, allows the imaging zone to be independently defined for each angular position of the source. For detector coordinates $(u,0)$, the corresponding ray angle with respect to the source-to-center line is

$$\alpha_u = \tau + \arctan\frac{u - R\sin\tau}{D_\tau} \tag{1}$$

with $D_\tau = R_D + R\cos\tau$ the source-to-detector distance. If we let $\alpha_{\min}$ and $\alpha_{\max}$ denote the $\alpha_{u_{\min}}$ and $\alpha_{u_{\max}}$ angles, respectively, the fan-beam in the central plane spans from $\alpha_{\min}$ to $\alpha_{\max}$ and its central ray makes an angle $(\alpha_{\min}+\alpha_{\max})/2$ with respect to the source-to-center line. The main purpose of the independent source and detector rotations is to be able to center the fan-beam and, therefore, the FOV, on a point $\mathbf{c} = (x_c, y_c, 0)$ that is not necessarily the center-of-rotation $\mathbf{o}$. We refer to this situation as the *offset FOV* in the following. For a given source position $\mathbf{s}_\beta$, the angle between the source-to-center line and the ray that passes through $\mathbf{c}$ is, using the law of sines in the triangle defined by the vertices $\mathbf{o}$, $\mathbf{s}_\beta$, and $\mathbf{c}$,

$$\alpha_c = \arcsin\left(\frac{x_c\cos\beta + y_c\sin\beta}{\|\mathbf{s}_\beta - \mathbf{c}\|}\right) \tag{2}$$

with $\alpha_c \in (-\pi/2, \pi/2)$ under the practical constraint $\|\mathbf{c}\| < R$. Centering the fan-beam on point $\mathbf{c}$ corresponds to having $\alpha_c = (\alpha_{\min}+\alpha_{\max})/2$, from which, recalling from Eq. (1) that $\alpha_{\min}$ and $\alpha_{\max}$ depend on τ, the detector tilt τ is implicitly defined in terms of α_c. For a given offset FOV center $\mathbf{c}$, we solved for τ numerically for each source position $\mathbf{s}_\beta$. We illustrate six source and detector positions of an example offset FOV in Fig. 3.

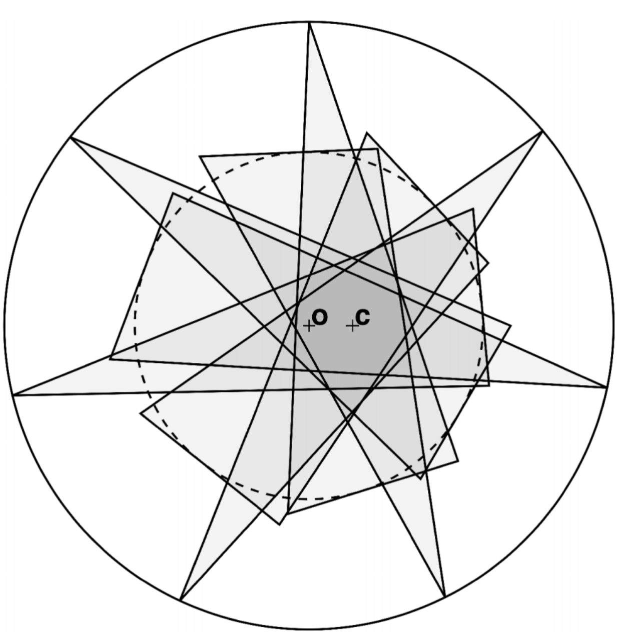

FIG. 3. Few-view example of an offset FOV in the central slice. The drawing corresponds to the ImagingRing up to a scaling factor. For each of the seven source positions, the detector is placed so that the fan-beam in the central slice is centered around $\mathbf{c}$. The center of the offset FOV $\mathbf{c}$ is at a distance $R/7$ from the center-of-rotation $\mathbf{o}$ as in the simulation results presented in this paper.

Ideally, the source rotation speed should be adjusted to provide regular angular sampling at $\mathbf{c}$, the center of the offset FOV. Then, from each (irregularly sampled) source position β, the angle α_c can be calculated using Eq. (2), and the coupled tilt angle τ computed from α_c. The tilt angles then determine the motion of the detector with respect to the source.

2.C. Reconstruction

CT reconstruction aims at finding the unknown patient density $f(\mathbf{x})$ at (x,y,z) from the projection value $g(\beta,u,v)$ for the ray from the source to the (u,v) position on the detector which are linked by

$$g(\beta,u,v) = \int_0^\infty f(\mathbf{s}_\beta + l\,\mathbf{r}_{\beta,u,v})dl, \tag{3}$$

where $\mathbf{r}_{\beta,u,v}$ is the unit vector from the source $\mathbf{s}_\beta$ to the (u,v) position on the detector.

We first concentrate on the 2D central slice, i.e., the source trajectory plane $z=0$, because it is the only part of space that satisfies the sufficiency condition of Tuy for exact reconstruction.[10] We have shown[6] that a suitable change of variable in the filtered-backprojection formula for conventional fan-beam CT (Ref. 11) results in the reconstruction formula

$$f(x,y,0) = \frac{1}{2}\int_0^{2\pi}\frac{1}{U^2}\int_{\mathbb{R}}\cos\alpha_u\frac{R}{D_\tau}g(\beta,u,0)h(u^*-u)\mathrm{d}u\,\mathrm{d}\beta \tag{4}$$

with

$$U = \frac{R\cos\tau + (x,y)\cdot(\sin(\tau+\beta), -\cos(\tau+\beta))}{D_\tau} \tag{5}$$

the weight used during backprojection, $u^* = R\sin\tau + [(x,y)\cdot(\cos(\tau+\beta),\sin(\tau+\beta)) - R\sin\tau]/U$ the cone-beam projection of the point $(x,y,0)$ onto the u-axis and h the usual ramp filter

$$h(u) = \int_{\mathbb{R}}|k_u|\exp(2\pi i u k_u)\mathrm{d}k_u. \tag{6}$$

The resulting algorithm is very close to the filtered-backprojection algorithm for conventional fan-beam CT since it consists of the following steps:

1. weighting the projections g by $(R/D_\tau)\cos\alpha_u$,
2. filtering the weighted projections by the usual ramp filter h,
3. backprojecting the filtered projections with a $1/U^2$ weight, i.e., the squared ratio of the source-to-detector distance to the distance between the source and the plane parallel to the detector that contains point $(x,y,0)$.

Our objective is to achieve a 3D reconstruction equivalent to that of the Feldkamp algorithm[8] which is commonly used for circular cone-beam CT. The Feldkamp algorithm performs filtering along parallel rows on the detector before backprojection, and the detector is assumed to be placed at the center of rotation, parallel to the tangent direction of the corresponding source position. For each parallel line on the Feldkamp detector, we consider the plane containing this line and the source. The common axis of this sheaf of planes lies at the source, oriented in the tangent direction of the source.

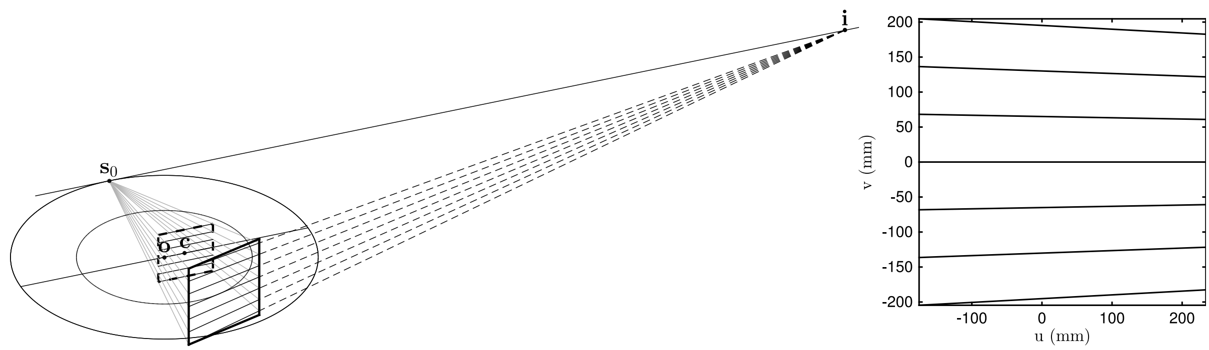

FIG. 4. Left: Illustration of the 3D effect when changing geometry from the Feldkamp detector (thick dashed line) to the ImagingRing detector (thick solid line). The drawing corresponds to the top source position ($\beta = 0$) in Fig. 3. The parallel rows of the Feldkamp detector project to a set of lines that are not parallel and intersect at point $\mathbf{i}$ which is at a distance $5R$ from the source $\mathbf{s}_0$. Right: 2D drawing of the same lines on the ImagingRing detector.

When intersecting this sheaf of planes with the tilted detector, the corresponding lines are no longer parallel, but converge on the point of intersection of the tilted detector plane with the axis of the sheaf, as illustrated in Fig. 4. The point of convergence is $\mathbf{i} = (D_\tau/\sin\tau, R, 0)$ if $\beta = 0$ (rotated accordingly if $\beta \neq 0$).

The nonparallel lines on the tilted detector cause difficulties when trying to mathematically convert the conventional geometry of the Feldkamp algorithm to the ImagingRing geometry. In the Feldkamp algorithm, ramp filtering of the projection values always occurs separately inside each plane of the sheaf, so there is little hope to achieve an equivalent filtering on the tilted detector other than filtering along the nonparallel lines. Since the maximum angle between the nonparallel filtering lines is small (for the modest tilt angles we consider), we have chosen to neglect this angle. Under this assumption, filtering can be kept along the rows of the ImagingRing projections and the resulting reconstruction formula is

$$f(x,y,z) \simeq \frac{1}{2}\int_0^{2\pi} \frac{1}{U^2}\int_{\mathbb{R}} \cos\alpha_{uv^*}\frac{R}{D_\tau} g(\beta,u,v^*)h(u^*-u)\,\mathrm{d}u\,\mathrm{d}\beta \tag{7}$$

with $v^* = z/U$ the v-component of the cone-beam projection of the point (x,y,z) onto the detector and $\cos\alpha_{uv^*} = \mathbf{r}_{\beta,u,v} \cdot (\sin\beta, -\cos\beta, 0)$ the cosine of the angle between the central ray passing by $\mathbf{o}$ and the ray that intersects the coordinate (u,v^*) on the projection. The approximation of this formula covers both the approximation of the Feldkamp formula and the additional approximation when filtering along the detector rows instead of the nonparallel lines described in Fig. 4. For nonuniform speed of the source, Eq. (7) is still applicable with the understanding that the integral over β is treated accordingly. A simple weighting can be applied at each β to account for nonuniform sampling. For example, $\mathrm{d}\beta$ can be interpreted as $(\mathrm{d}\beta/\mathrm{d}t)\mathrm{d}t$ so the instantaneous speed of the source rotation is used as the weight at position β.

2.D. Numerical simulations and real data

The resulting algorithm has been evaluated on simulated and real projection data using an open-source implementation in the Reconstruction Toolkit.[12] The simulations used geometry parameters that were close to the ImagingRing geometry: $R = 70$ cm, $R_D = 40$ cm, $u_{\min} = -17.53$ cm, $u_{\max} = 23.39$ cm, $v_{\max} = 20.46$ cm. A total of 720 projections were simulated with 1024×1024 pixels. An offset FOV acquisition of the 3D Shepp Logan phantom[11] was simulated with the offset FOV centered at point $\mathbf{c} = (0,-10,0)$ cm which resulted in a range of detector tilt τ angles from $-25.3°$ to $17.6°$. With respect to the parallel lines on the detector along which filtering was performed, the largest angle approximation to the correct filtering line was $5.1°$. The source speed was constant, i.e., β was uniformly sampled in the range $[0, 2\pi]$.

The same simulations were repeated with Poisson noise. The Shepp Logan densities were weighted by $0.018\,79$ mm^{-1}, i.e., the linear attenuation coefficient of water at 75 keV. The number of photons received per detector pixel without object in the beam was constant for all pixels in both geometries and equal to 10^7. With this beam fluence, the minimum number of photons received by a detector pixel after attenuation was 35×10^4.

Another digital phantom was used to evaluate the *cone-beam artifact*, i.e., the impact of missing data for exact reconstruction which increases with the distance to the plane of the source trajectory. The phantom was the disk phantom described by Kudo *et al.*[13] on one side of the plane of the source trajectory and, on the opposite side but in the same cylinder with density 1 and radius 10.2 cm, an 8^3 cm^3 cube centered at $(0,-10,6)$ cm and with a density equal to 2.

For comparison, projections of a conventional detector were also simulated and reconstructed with the Feldkamp algorithm using the same source positions and a larger detector because the same detector in Feldkamp's geometry can only image a disk with a 9.7 cm radius in the central slice. The detector size for the conventional geometry was 1700×1024 pixels of 0.25^2 mm^2 to fully image the phantoms at each angle in the central slice.

Real projection data were acquired on a prototype ImagingRing. The offset FOV was centered at two positions, $\mathbf{c} = (0,0,0)$ cm and $\mathbf{c} = (0,-8.5,0)$ cm where an anthropomorphic head phantom (Proton Therapy Dosimetry Head; CIRS, Norfolk, VA) was placed. Precalibrated geometric parameters and flat-field correction images were provided by the ImagingRing Software Suite (ImRiSS, commissioning modules) according to the measured source and detector angles of each projection. The geometric calibration uses a 9 DOFs look-up table: 3 DOFs for the source position in look-up tables parametrized by the angle β of the source arm, and 6 DOFs for the detector position and orientation in look-up tables parametrized by the angle $\beta+\tau$ of the detector arm. These look-up tables are independent of the offset FOV center, i.e., the position of the source does not influence the geometric parameters of the detector and conversely. The average (standard deviation) values of the main geometrical parameters were $R = 63.9(0.5)$ cm, $R_D = 40.2(0.2)$ cm, $u_{\min} = -18.1(0.2)$ cm, $u_{\max} = 22.9(0.2)$ cm, $v_{\max} = 20.5(0.2)$ cm. The sensitive area of the ImagingRing detector is not centered in the u direction due to mechanical constraints posed by its lateral electronics. The design of the source and the detector trajectory was left to the ImRiSS which also accounts for mechanical constraints of the system and resulted in a range of detector tilt angles τ from $-24.1°$ to $16.6°$ for the offset FOV. Conventional preprocessing of the measured projection images was used: the heuristic truncation correction of Ohnesorge *et al.*,[14] the scatter correction algorithm of Boellaard *et al.*[15] with a scatter-to-primary ratio of 20% to compensate for the lack of antiscatter grid, and a Hann window during ramp filtering. The x-ray tube parameters were 120 kV voltage, 0.3 mm focal spot size, and 0.2 mAs exposure per projection. The pixel number and size were the same as in the simulation. The number of projections was 600 acquired at a frame rate of 10 Hz with an average rotation speed of 6.2°/s which was varied to sample regularly rays going through the offset FOV center within the motor drives' constraints of the ImagingRing.

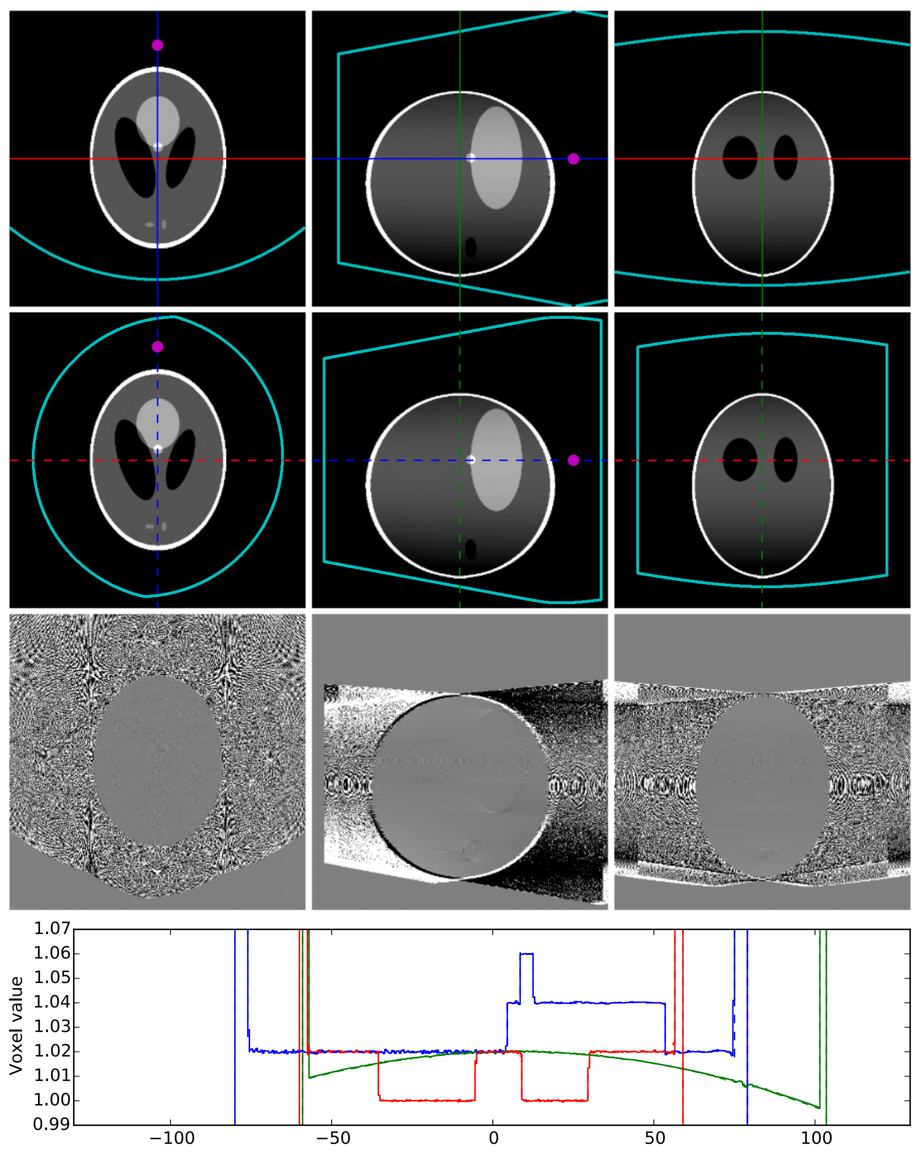

FIG. 5. Axial (left column), sagittal (middle column), and coronal (right column) slices of the Shepp Logan simulation results using Feldkamp projections and algorithm (top row, grayscale window [1, 1.06]), ImagingRing projections and algorithm (second row, grayscale window [1, 1.06]) and their difference (third row, grayscale window [−0.005, 0.005]). The last row contains plots through the lines drawn on each slice with a corresponding color and style, i.e., solid lines for the Feldkamp images and dashed lines for the ImagingRing images. The cyan contour delimits the FOV and the magenta point is the center-of-rotation of the system.

3. RESULTS

The cone-beam CT images obtained from the noiseless sets of simulated projections of the Shepp Logan phantom are compared in Fig. 5. The results were very similar for the original Feldkamp algorithm applied to projections simulated with a detector perpendicular to the source-to-center line (first row) compared to the new filtered backprojection algorithm for the ImagingRing (second row). The comparative plots are so close that it is difficult to distinguish the dashed lines from the solid lines (last row). A narrow window corresponding to just 10 Hounsfield Units (HU) was used to visualize some differences (third row). The largest differences, outside the phantom, were attributed to digital noise introduced, e.g., by the linear interpolation during backprojection. Small differences are distinguishable in the phantom around structures which increase with the distance to the central plane and are presumed to be caused by the tilt of the filter direction which has not been accounted for (Fig. 4). However, these differences are negligible compared to the so-called cone-beam artifact which also increases with the distance away from the central plane and is equally visible in the two cone-beam CT images. This cone-beam artifact, caused by missing data for exact reconstruction, is well known and has been studied in many works.[16,17] The Shepp Logan experiments were repeated with Poisson noise and the result is shown in Fig. 6. The visual effect and profiles of the noise were similar in both configurations.

The results with the other digital phantom in Fig. 7 showed larger differences but the conclusions are similar. Missing data caused another type of cone-beam artifacts, i.e., the distortion of the cube and the disks in both Feldkamp and the new reconstruction algorithms. This was expected for this phantom which is very sensitive to missing data in circular source trajectory (the disk phantom has been designed to illustrate these missing data artifacts in cone-beam CT reconstruction with a circular source trajectory). Differences between the two reconstruction algorithms are mainly visible in the difference image with a 200 HU window (Fig. 7, third row) but these differences are less visible than the cone-beam artifacts in both reconstructed images (Fig. 7, first two rows). As expected, the difference between the two algorithms is mainly visible in the sagittal slice, because the projection images parallel to the sagittal slice (for $\beta = -\pi/2$ and $\beta = \pi/2$) have the largest approximation regarding the direction of the ramp filter (Fig. 4) whereas the direction of the filter is the same in the two algorithms for the projection images parallel to the coronal slice (for $\beta = 0$ and $\beta = \pi$), i.e., parallel to the plane of the source trajectory.

The imaging of a real phantom confirmed that the image quality is visually similar with a centered and an offset FOV (Fig. 8). The two cone-beam CT images clearly depict the phantom anatomy even though there are residual artifacts that are typical of cone-beam CT images: statistical noise, beam hardening, scatter, etc. Streaks in the vertebræ region of both

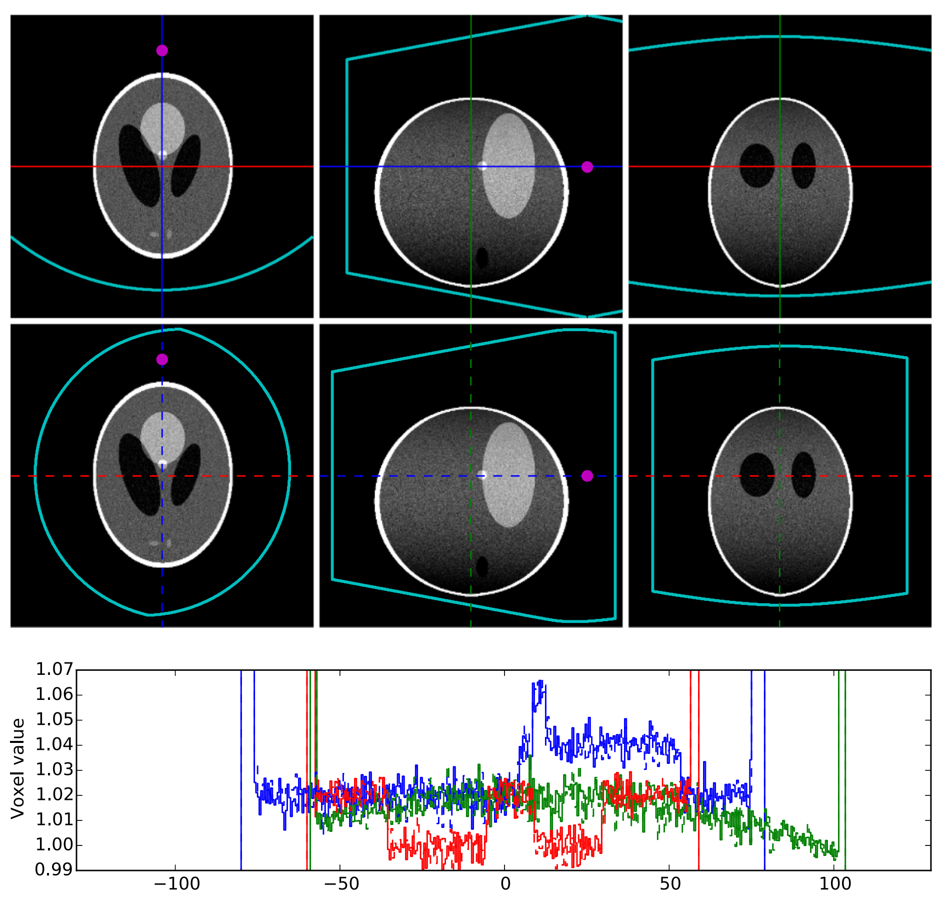

FIG. 6. Results from Shepp Logan projections with Poisson noise. The presentation is the same as Fig. 5 without the difference row.

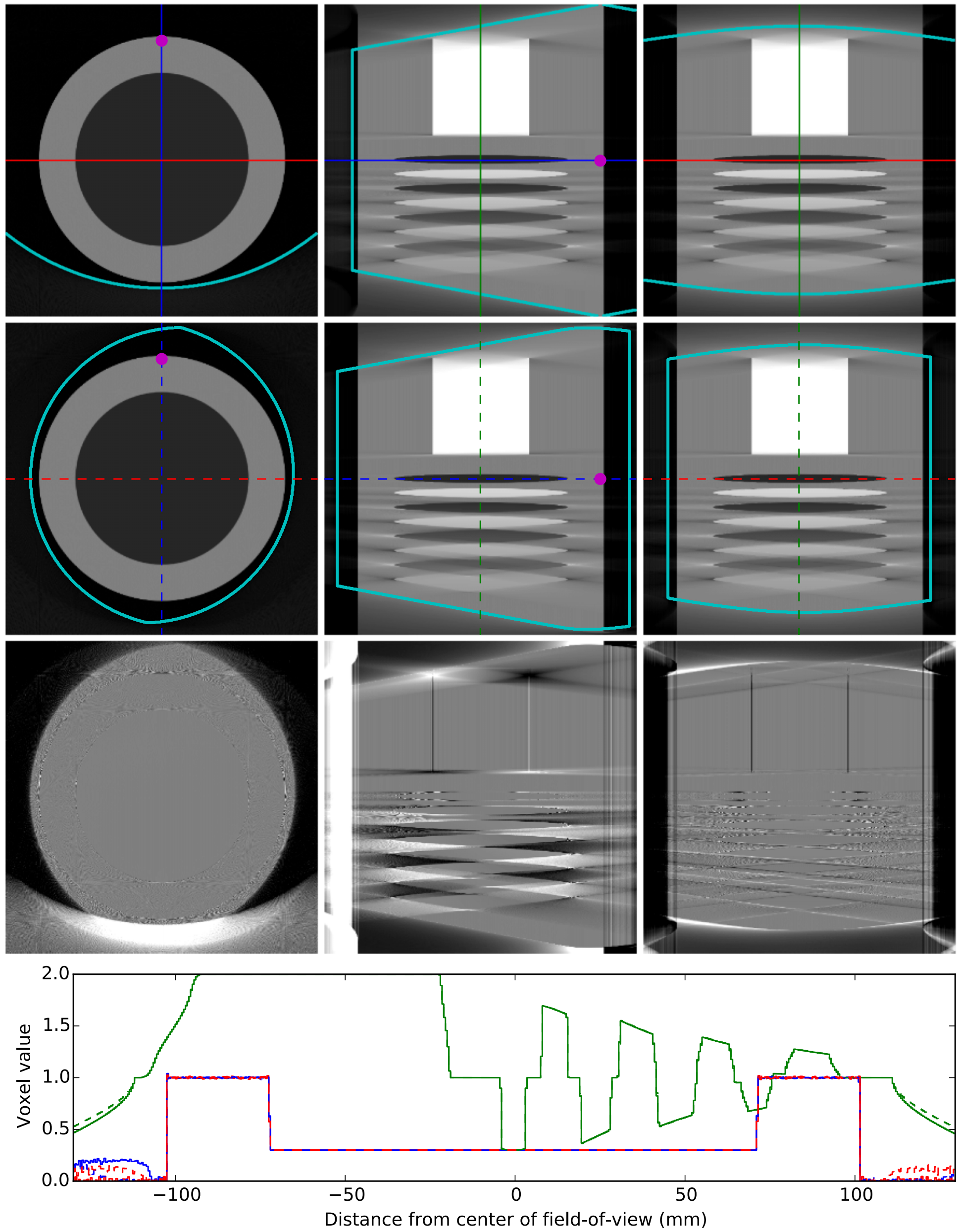

FIG. 7. Idem as Fig. 5 with the second digital phantom. The grayscale window is $[0,2]$ for the first two rows and $[-0.1,0.1]$ for the last row of differences.

images could also be cone-beam artifacts, similar to those appearing in the second digital phantom (Fig. 7).

The offset FOVs are drawn in all CT slices of Figs. 5–8 with a cyan contour using the source and detector as the imaging zone. They have been computed numerically by selecting the voxels that are in the imaging zone for every source position. They illustrate the ability of the ImagingRing to image a specific region of space with an offset FOV with respect to the center-of-rotation (magenta point). A much larger FOV has been obtained with the Feldkamp geometry at the top of Figs. 5–7 but there is no commercial detector that would have the required size, i.e., 85 cm-wide detector at a distance $R+R_D = 110$ cm from the source. The lemon shape of the ImagingRing FOVs in the central slice (left column of Fig. 5 and top-left slice of Fig. 8) is unusual but can be understood from Fig. 3: the fan-beam captures an angular range that will depend on the detector tilt τ and the distance between the source and the FOV center.

4. DISCUSSION

A filtered-backprojection algorithm has been proposed to reconstruct CT images from sequences of projections where the source and the detector follow a circular trajectory but rotate independently for the purpose of imaging an offset FOV. The reconstruction is similar to the Feldkamp algorithm, without derivatives of the geometrical parameters, unlike the algorithm of Crawford *et al.*,[7] and requires three steps: projection weighting, ramp filtering, and a weighted backprojection [Eq. (7)]. The computational cost is negligible with respect to the Feldkamp algorithm because the only difference, the new projection weighting, takes only 5% of the

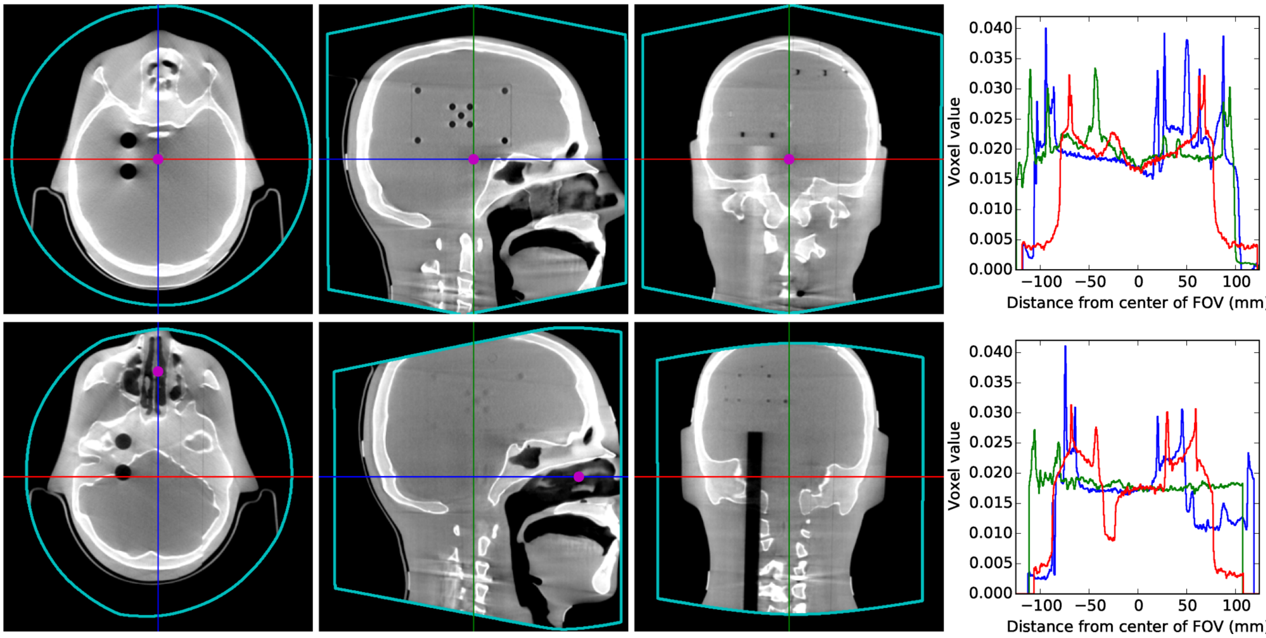

FIG. 8. Axial (first column), sagittal (second column), and coronal (third column) slices of cone-beam CT images of a head phantom with a centered FOV (first row) and an offset FOV (second row). Profiles of the images along the lines drawn on each slide with corresponding colors are provided in the fourth column. The cyan contour delimits the FOVs and the magenta point is the center-of-rotation of the system. Note that the phantom has been moved between the two acquisitions.

total reconstruction time in our implementation. Furthermore, the reconstruction can start as soon as the first projections are available, while other projections are still being acquired.

Our experiments indicated that the image quality is nearly identical to that obtained from the Feldkamp algorithm (Fig. 5). However, the two procedures are not mathematically equivalent except in the central slice; elsewhere, parallel rows of the detector in the conventional Feldkamp geometry project onto lines on the tilted detector that converge on a common point (Fig. 4) and we have neglected the inclination of the filter along these nonparallel lines. If oblique filtering were used, the inversion formula would be equivalent to Feldkamp's with the same mathematical properties, e.g., the preservation of the integral along lines parallel to the rotation axis or its exactness for objects densities independent of the rotation axis z (see Appendix A of Feldkamp *et al.*[8]). However, filtering these lines is difficult without resampling and avoiding resampling is the main benefit of the proposed algorithm. Neglecting the inclination of these lines is reasonable because the inclination angles are small (5° or less) in the ImagingRing configuration and filtering along the rows of the ImagingRing detector proved to have an indiscernible impact compared to the Feldkamp algorithm in our simulations. More simulated experiments are required to further evaluate the impact of this approximation on numerical phantoms which are closer to clinical cases.

Simulations with Poisson noise show similar behavior of the proposed algorithm as the Feldkamp algorithm when the same number of photons was emitted toward each detector pixel in the Feldkamp and the ImagingRing configurations (Fig. 6). This is consistent with the fact that the main source of noise enhancement in the two filtered-backprojection algorithms is the same ramp filter [Eq. (6)]. Noise in real datasets would also depend on the number of photons received per detector pixel with no object which will change due to variations in the solid angle of the x-ray beam seen by a pixel with the detector tilt τ and variations in the source fluence with the angle α between the source-to-center line and the source-to-pixel line due to the so-called heel effect, i.e., heterogeneity of the x-ray beam fluence.

The application of the algorithm to a real dataset demonstrated that the new algorithm [Eq. (7)] produces a cone-beam CT image with a quality which is visually similar to cone-beam CT images acquired with a conventional geometry (Fig. 8). It seems that other artifacts related to the x-ray physics and the quality of the detector overwhelm reconstruction artifacts such as the cone-beam artifact. The correction of detector lag, beam hardening, scatter, and all other phenomena causing artifacts in cone-beam CT images is still an active field of research that will benefit the reconstruction of cone-beam CT images acquired with the ImagingRing.

The limited size of the detector presents a difficulty with both the conventional and the ImagingRing geometries because the Feldkamp algorithm and the new algorithm assume that there is no lateral truncation, which is not a safe assumption when imaging with a 41 cm-wide detector. One solution that is used in existing cone-beam CT scanners for radiotherapy is to translate the detector before the acquisition because axial truncation on one side can then be handled using an appropriate weighting scheme which exploits redundancies in the projections after a full revolution.[9] Similar approaches are being investigated for the ImagingRing but the independent rotations can be used instead of in-plane detector translation such that only a small portion of space around the offset FOV center is imaged by all source positions but a larger portion of space is seen by the x-ray

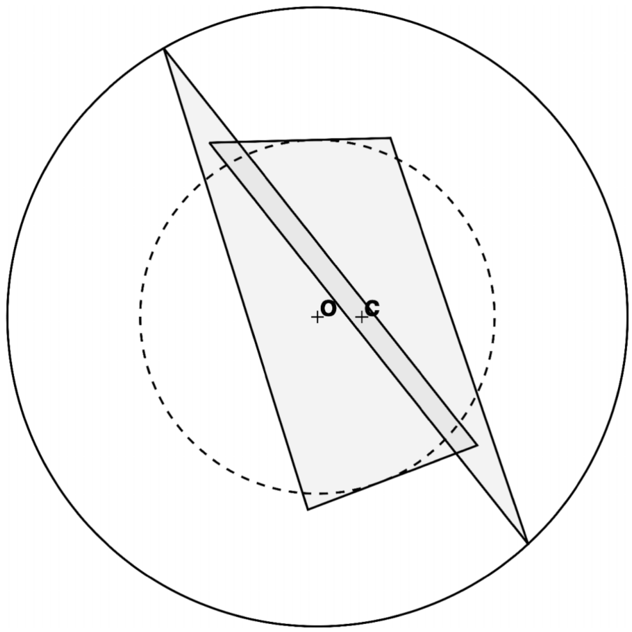

FIG. 9. Two-view example of an enlarged offset FOV in the central slice using the independent rotations of the source and the detector. Only a small disk around the offset FOV center **c** would be seen by all source positions but a larger FOV would be reconstructible than in Fig. 3 with an adequate weighting scheme for redundancies in the acquisition, following Cho *et al.* (Ref. 9).

source over more than 180°, as illustrated in Fig. 9. This ImagingRing-specific solution for larger FOVs introduces new geometrical aspects to the data redundancy problem and new weighting schemes will be required. The reconstruction algorithm presented here would still be used after suitably weighting the projections. If truncation cannot be avoided with this technique, heuristic corrections can be used[14] but there are also on-going investigations in new reconstruction algorithms that can correctly handle some degree of lateral truncation.[18]

5. CONCLUSION

We have proposed a 3D filtered backprojection algorithm for the reconstruction of cone-beam CT images acquired with independent rotation of the source and detector. The new algorithm has been successfully applied to simulated and real data where the FOV was not centered on the center-of-rotation of the system. This work forms a substantial basis for clinical translation of novel imaging protocols in IGRT using the offset FOV feature of the ImagingRing scanner.

ACKNOWLEDGMENTS

This work was partially supported by Grant Nos. ANR-12-BS01-0018 (DROITE project) and ANR-13-IS03-0002-01 (DEXTER project) from the Agence Nationale de la Recherche (France) and I 1383-B23 (DEXTER project) of the Austrian Science Fund (FWF). This work was performed within the framework of the LABEX PRIMES (No. ANR-11-LABX-0063) of Université de Lyon, within the program "Investissements d'Avenir" (No. ANR-11-IDEX-0007) operated by the French National Research Agency (ANR). The author Philipp Steininger is heading the research and development department at medPhoton GmbH.

[a)]Author to whom correspondence should be addressed. Electronic mail: simon.rit@creatis.insa-lyon.fr

[1]L. Dawson and M. Sharpe, "Image-guided radiotherapy: Rationale, benefits, and limitations," Lancet Oncol. **7**, 848–858 (2006).
[2]D. Verellen, M. De Ridder, N. Linthout, K. Tournel, G. Soete, and G. Storme, "Innovations in image-guided radiotherapy," Nat. Rev. Cancer **7**, 949–960 (2007).
[3]D. Jaffray, J. Siewerdsen, J. Wong, and A. Martinez, "Flat-panel cone-beam computed tomography for image-guided radiation therapy," Int. J. Radiat. Oncol., Biol., Phys. **53**, 1337–1349 (2002).
[4]P. Grangeat, R. Guillemaud, P. Rizo, R. Sauze, Q. Donner, and J. Gorius, "Cone-beam SPECT with a tilted detector," Comput. Med. Imaging Graphics **17**, 279–287 (1993).
[5]G. Gullberg, C. Crawford, and B. Tsui, "Reconstruction algorithm for fan beam with a displaced center-of-rotation," IEEE Trans. Med. Imaging **5**, 23–29 (1986).
[6]S. Rit and R. Clackdoyle, "2D filtered backprojection for fan-beam CT with independent rotations of the source and the detector," in *Third International Conference on Image Formation in X-ray Computed Tomography*, *Salt Lake City, UT* (2014), pp. 249–252, see http://ct-meeting.org/data/ProceedingsCTMeeting2014.pdf.
[7]C. Crawford, G. Gullberg, and B. Tsui, "Reconstruction for fan beam with an angular-dependent displaced center-of-rotation," Med. Phys. **15**, 67–71 (1988).
[8]L. Feldkamp, L. Davis, and J. Kress, "Practical cone-beam algorithm," J. Opt. Soc. Am. A **1**, 612–619 (1984).
[9]P. Cho, A. Rudd, and R. Johnson, "Cone-beam CT from width-truncated projections," Comput. Med. Imaging Graphics **20**, 49–57 (1996).
[10]H. Tuy, "An inversion formula for cone-beam reconstruction," SIAM J. Appl. Math. **43**, 91–100 (1983).
[11]A. Kak and M. Slaney, *Principles of Computerized Tomographic Imaging* (IEEE, New York, NY, 1988).
[12]S. Rit, M. Vila Oliva, S. Brousmiche, R. Labarbe, D. Sarrut, and G. Sharp, "The Reconstruction Toolkit (RTK), an open-source cone-beam CT reconstruction toolkit based on the Insight Toolkit (ITK)," J. Phys.: Conf. Ser. **489**, 012079 (2014).
[13]H. Kudo, F. Noo, and M. Defrise, "Cone-beam filtered-backprojection algorithm for truncated helical data," Phys. Med. Biol. **43**, 2885–2909 (1998).
[14]B. Ohnesorge, T. Flohr, K. Schwarz, J. Heiken, and K. Bae, "Efficient correction for CT image artifacts caused by objects extending outside the scan field of view," Med. Phys. **27**, 39–46 (2000).
[15]R. Boellaard, M. van Herk, H. Uiterwaal, and B. Mijnheer, "Two-dimensional exit dosimetry using a liquid-filled electronic portal imaging device and a convolution model," Radiother. Oncol. **44**, 149–157 (1997).
[16]P. Rizo, P. Grangeat, P. Sire, P. Lemasson, and P. Melennec, "Comparison of two three-dimensional x-ray cone-beam-reconstruction algorithms with circular source trajectories," J. Opt. Soc. Am. A **8**, 1639–1648 (1991).
[17]S. Bartolac, R. Clackdoyle, F. Noo, J. Siewerdsen, D. Moseley, and D. Jaffray, "A local shift-variant Fourier model and experimental validation of circular cone-beam computed tomography artifacts," Med. Phys. **36**, 500–512 (2009).
[18]R. Clackdoyle and M. Defrise, "Tomographic Reconstruction in the 21st Century. Region-of-interest reconstruction from incomplete data," IEEE Signal Process. Mag. **27**, 60–80 (2010).